

Deep generative model super-resolves spatially correlated multiregional climate data

Norihiro Oyama,^{1,*} Noriko N. Ishizaki,² Satoshi Koide,¹ and Hiroaki Yoshida¹

¹*Toyota Central R&D Labs, Inc., Bunkyo-ku, Tokyo 112-0004, Japan*

²*Center for Climate Change Adaptation, National Institute for Environmental Studies, Tsukuba 305-8506, Japan*

(Dated: September 27, 2022)

Super-resolving the coarse outputs of global climate simulations, termed downscaling, is crucial in making political and social decisions on systems requiring long-term climate change projections. Existing fast super-resolution techniques, however, have yet to preserve the spatially correlated nature of climatological data, which is particularly important when we address systems with spatial expanse, such as the development of transportation infrastructure. Herein, we show an adversarial network-based machine learning enables us to correctly reconstruct the inter-regional spatial correlations in downscaling with high magnification up to fifty, while maintaining the pixel-wise statistical consistency. Direct comparison with the measured meteorological data of temperature and precipitation distributions reveals that integrating climatologically important physical information is essential for the accurate downscaling, which prompts us to call our approach π SRGAN (Physics Informed Super-Resolution Generative Adversarial Network). The present method has a potential application to the inter-regionally consistent assessment of the climate change impact.

I. INTRODUCTION

The increase of greenhouse gases in the air composition due to human activities is now believed to have led to the rise in the frequency of unusual disasters [1–4]. To prevent an irreversible collapse of the current ecosystem and resulting impoverishment of human lives, many countries have set specific medium- and long-term goals for the reduction of greenhouse gas emissions, and similar paradigm shifts in decision making have occurred even at the private sector level.

Numerical approaches are regarded as the most powerful and reliable scientific option at the moment in quantitatively evaluating the efficacy of political or management plans that aim to tackle climatological issues. The Global Climate Model (GCM) is the prime example, which has accurately reproduced past and current climate changes, and its reliability of quantitative future estimates is sufficiently high [5]. Such future projections with high accuracies rely on the overall consideration of the global atmospheric and oceanic circulation (and even still more complicated ingredients such as chemical [6] and biological [7] processes) [8–12], and thus, the horizontal spatial resolution is sacrificed by the required computational costs; the typical resolution of the GCMs is only down to the order of one degree in longitude and latitude, corresponding to a grid size of more than a hundred kilometers on the equator. Therefore, to exploit the GCM outputs to assess the impact of climate change and to make proper decisions, it is obviously vital to super-resolve the coarse grid spacing of simulations and to reach the fine resolution of interest. Here, special attention should be given to reproducing the inherent spatial correlation of the meteorological variables, as well as the local statistics, in decision making by integrating multire-

gional information [13–17], such as transportation infrastructure development and sustainable energy networks, future urbanization, and agricultural intensification.

A variety of techniques to super-resolve GCM outcomes, which are referred to as the *downscaling* (DS) methods in meteorology and climatology, have been developed [18–25]. They are categorized roughly into two groups: dynamical [18–21] and statistical DS methods [22–25]. The dynamical downscaling method is based on physical footings: several coupled differential equations are numerically integrated with the results of the GCM (or any other crude-resolution simulation results) being used as the boundary conditions. However, the computational cost again creates a trade-off between the accuracy and the feasibility. In contrast, in the statistical approaches, we turn a blind eye to the physical laws behind the data. Instead, empirical links between the large- and local-scale climates are identified and applied to the crude-resolution climate model outputs. Since the systematic errors of the naively interpolated GCM output (referred to as the bias) are locally corrected such that the statistical properties are precisely reproduced, the spatial correlation, i.e., the information on the events occurring at distant places, is discarded [26–28]. The statistical downscaling methods overcoming the latter problem remain to be developed.

In this paper, we propose a machine learning approach that super-resolves the GCM outputs and reproduces both the local statistics and the instantaneous spatial correlations between distant regions. Our method is based on the generative adversarial network (GAN) approach, which has been proven to be a very powerful downscaling tool through several previous studies [29, 30]. To accurately reproduce the physical nature, we use auxiliary but climatologically important input data, topographic information and sea-level pressure distributions, in addition to the target variables, temperature and precipitation distributions (see Fig. 1A). Since the present method falls within the criteria of the first-

* Norihiro.Oyama.vb@mosk.tytlabs.co.jp

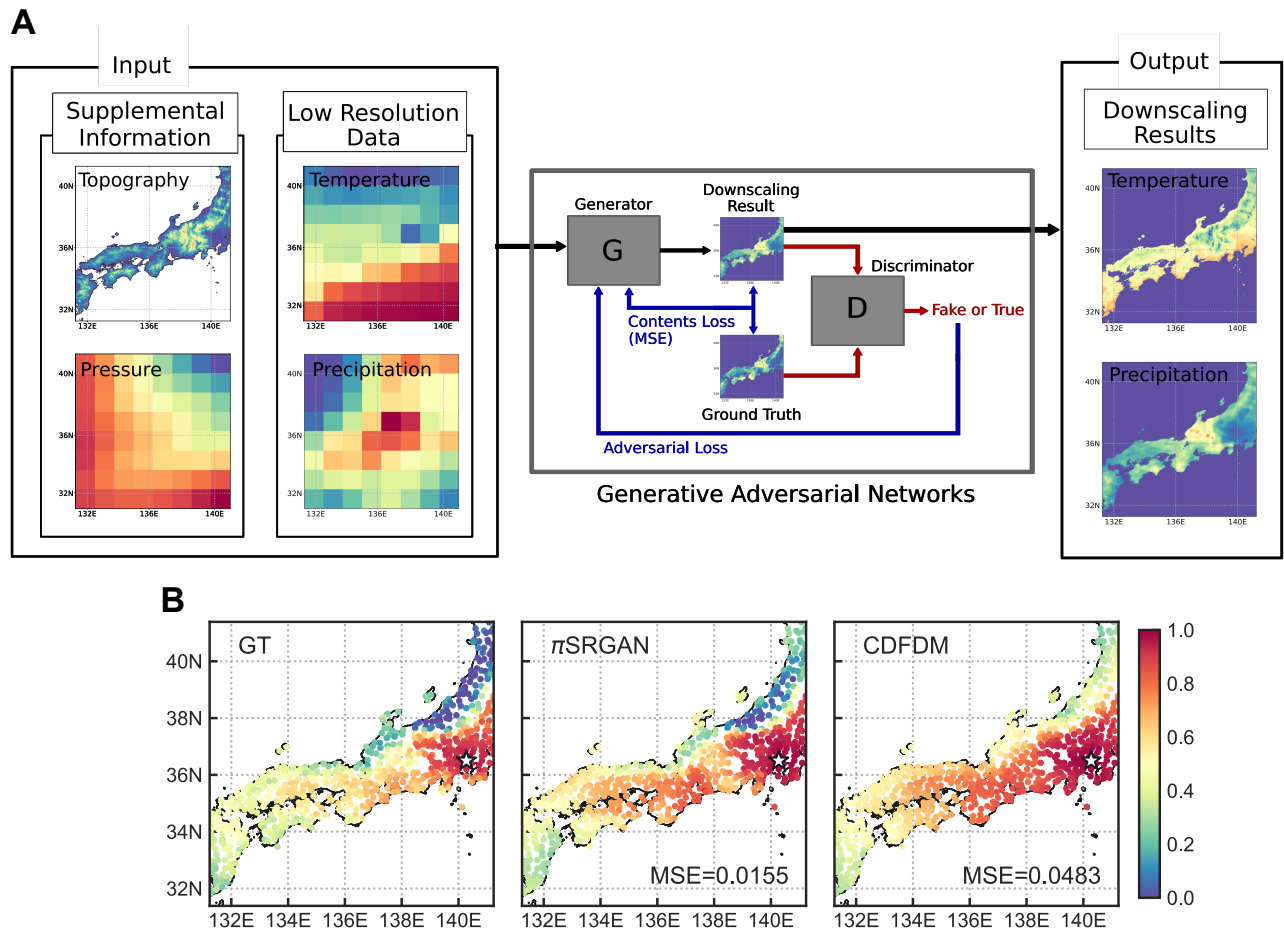


FIG. 1. Schematic diagram of π SRGAN and the distribution of spatial correlation coefficients. (A) High-resolution topography and low-resolution sea level pressure, in addition to the low resolution data corresponding to the output, are input to the generative adversarial networks. (B) The reconstructed distributions of spatial correlation coefficients, indicating the correlation strength from the reference site at Tokyo [35.735°N, 139.6683°E], obtained with the present π SRGAN and the conventional CDFDM are compared to the ground truth (GT).

level physics informed super-resolution methods [31], we name our method π SRGAN (Physics Informed Super-Resolution Generative Adversarial Network). The direct comparison with the measured meteorological data shows that the local statistical properties are obtained using the practical output from the GCM simulation as accurately as the conventional statistical downscaling method that is focused on matching these properties. We then highlight that the spatial correlation of variables is accurately reproduced, which was achieved neither with conventional nor with other machine learning-based downscaling methods (see Fig. 1B). The present method is therefore the next generation downscaling method that has a potential application in climate change assessment considering both local-scale and interregional events.

II. RESULTS

A. π SRGAN: Physics-Informed Super-Resolution Generative Adversarial Networks

We employ a super-resolution method based on generative adversarial networks (Super-Resolution Generative Adversarial Networks: SRGAN, see Methods section for details) as the basic machine learning algorithm, which was proven to have potential in DS with a scale factor up to fifty [29]. Although the original SRGAN was able to restore physical consistency in the turbulent wind velocity field, which was shown in terms of the well-known Kolmogorov 5/3 power-law [35], it failed to reproduce the basic statistics, such as the precipitation probability [29] (as presented later in this article). Here, to accurately obtain both the basic statistics and the spatial correlation patterns, we introduce additional auxiliary physical information (Fig. 1A), which is used as hints for the DS

TABLE I. Summary of protocols compared in this study

Abbr. name	Explanation
GT	Ground truth (observation results offered by AMGSD [32])
LR	Low resolution data of JRA-55 [33]
SRGAN	Standard SRGAN-based method [29]
π SRGAN	Present method (Physics-Informed SRGAN)
CDFDM	Cumulative distribution function-based downscaling method [34]

of the variables of interest, i.e., temperature and precipitation. Since the use of supplemental physical information during learning is regarded as primary-level physics-informed machine learning [31], we call this method the Physics-Informed SRGAN (π SRGAN for short).

There are a vast variety of options for supplemental information, as seen in several similar recent attempts [30, 36–38]. Here, we carefully selected two meteorologically and climatologically important sets of auxiliary information: the topography and the sea-level pressure field. We note that the latter is included because it is one of the fundamental hydrodynamic (or aerodynamic) variables on which the various quantities of sub-models of GCMs are based, and it is described with fewer assumptions in the models than other meteorological variables such as humidity. In the literature, strong links between synoptic-scale horizontal circulation and vertical motion are discussed in terms of the sea-level pressure [39–42]. Under the assumption that the topography is identical over time, we used a high-resolution format for all DS procedures. In contrast, the pressure field that is input into the networks at the instant of the DS is in the low-resolution format obtained as the model prediction (e.g. of the GCMs).

The performance of π SRGAN is evaluated via direct comparisons with a couple of existing methods including a non-machine learning-based method: we summarize these methods in Table I. The cumulative distribution function-based downscaling method (CDFDM) is the widely used conventional statistical DS method (see the method section for the details), and the SRGAN refers to the original SRGAN-based method presented in Ref [29].

B. Data sets

We use the climate model simulation outputs for the low-resolution input and the real observation data for the high-resolution ground truths in the case studies. As the low-resolution data, we used the Japanese 55-year re-analysis (JRA-55) data from 1980 to 2018 [33] with data assimilation. The grid spacing is 1.25 degrees. The daily data corresponding to the reference data (in Japanese local time) were created from 3-hourly simulation data. Specifically, data at 0Z, 3Z, 6Z, 9Z and 12Z on the target

date and data at 15Z, 18Z and 21Z on the previous day of the target date were averaged to obtain the daily data in JST. The reference high-resolution data were the Agro-Meteorological Grid Square Data (AMGSD) [32]. The 1 km-meshed daily data over Japan are constructed using the in-situ observation network system of the Japan Meteorological Agency, which covers the entire land area over Japan from 122 to 146 degrees east and from 24 to 46 degrees north.

We chose the 6800 days of data for training, 600 for validation, and other 6800 for testing, out of 14245 days of data in total from 1980 to 2018, for both low-resolution (JRA-55) and high-resolution (AMGSD) data; the remaining data (45 days) were discarded. The AMGSD data were adjusted such that the grid spacing was 0.025 degrees/grid both in latitude and longitude. We extracted the data for the region from 130.625 to 140.625 degrees east and from 30.625 to 40.625 degrees north, which results in a 400×400 pixels square. The JRA-55 data of the corresponding region are 8×8 pixel squares, and thus, the scale factor for the DS tasks is 50.

C. Qualitative visualization

We first present typical qualitative visualizations for the temperature and the precipitation fields of one day in Fig. 2, which highlights the ambitious downscaling with the present large scaling factor of fifty. Here, the high-resolution information of 2500 pixels is extracted from one single pixel in the low-resolution counterpart. We compare the results of different protocols (summarized in Table I), along with the visualization of the original low-resolution JRA-55 and the high-resolution AMGSD data.

The difference in the downscaled temperature from the ground truth is not very large (the upper row of Fig. 2), although that of the SRGAN is slightly inferior to those of other methods. In contrast, the results for precipitation demonstrate rich information on the features of DS protocols (the lower row of Fig. 2). The CDFDM result shows an overly smoothed profile compared to the GT: high precipitation values (represented by red colors) are observed in a vaster area. On the other hand, the present π SRGAN finely reproduces the localized nature of the high precipitation areas, which the CDFDM

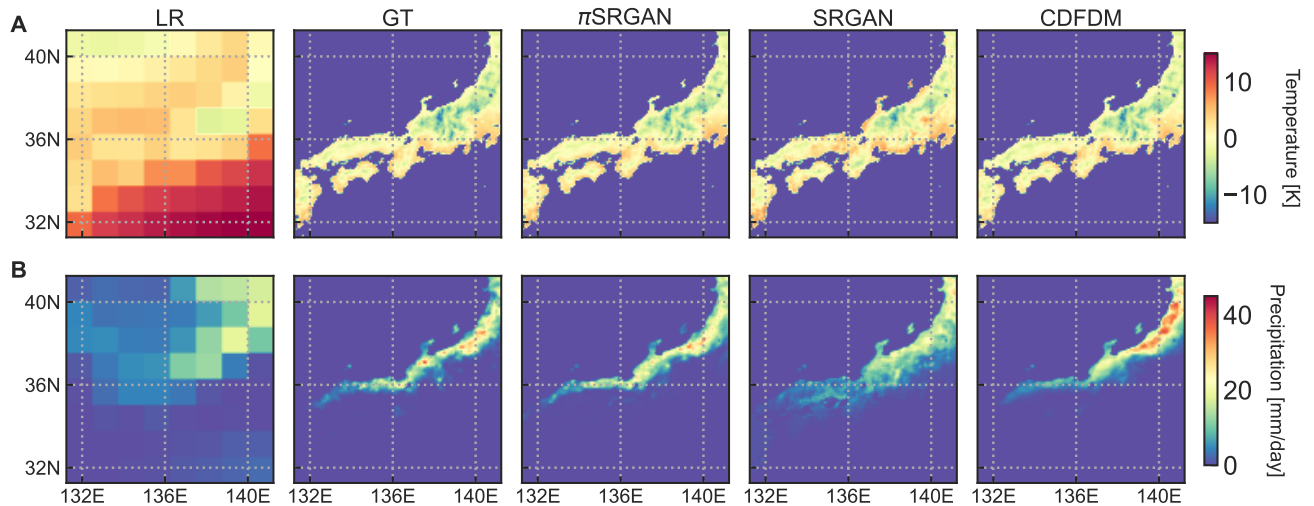


FIG. 2. Downscaling results. Distributions of temperature (A) and precipitation (B) obtained with the π SRGAN, SRGAN, and CDFDM are compared with the corresponding low-resolution (8×8) inputs (LR) and the high-resolution (400×400) ground truth (GT). The resolution of the downscaled images is the same as that of the GT. The data from January 24, 2008, are displayed.

fails to describe. Remarkably, the SRGAN also shows an overly smoothed precipitation field, although the GAN-based methods [13–17] are recognized to be advantageous in reproducing such fine structures; it exhibits a vast area with small precipitation values, whereas it hardly expresses the heavy rain events observed in the GT. We note that the maximum precipitation values of the π SRGAN and CDFDM are very close to that of the GT.

D. Single-site statistics

Here and in the following subsections, we discuss the statistical features of our downscaling results, focusing on the precipitation p , which is generally considered to be difficult to downscale accurately. In particular, we carefully examine the statistical consistency with the ground truth, which is crucial in actual usage of the DS results, e.g., in impact assessment of climate change in the future.

We first measure the probability distribution functions (PDFs) of the precipitation data at 12 representative sites, $P_S(p)$. Here, the PDFs are calculated using the set $\{p_k(l) | l \in \mathcal{S} \text{ and } k \in \mathcal{D}_{\text{test}}\}$, where \mathcal{S} stands for the site of interest (each site includes 100 grid points: see Table S3), $\mathcal{D}_{\text{test}}$ is the set of dates that are used for the test data, and $p_k(l)$ is the value of the precipitation at the pixel l and for the date k (we omit the subscript unless necessary below). The results are shown in Fig. 3 (A-L). The 12 sites in Fig. 3 are chosen from the seaside areas within the system boundary of this study, as depicted in Fig. 3(M). Table S3 provides more precise information (latitude, longitude, etc.) about these sites.

Overall, Fig. 3(A-L) shows that all methods express the regional dependence for light rainfalls of $p < 100$ mm/day. Regarding each method, the CDFDM provides results matching the GT very well, including the heavy rainfall regime where $p > 100$ mm/day up to the values at which $P^{\text{GT}}(p)$ becomes around 10^{-5} . This is expected because in the CDFDM the data are processed such that the resulting PDFs become completely consistent with the training data. If we shift our attention to the SRGAN results, the probabilities of observing intermediate values of precipitation (those residing in the $P(p) \approx 10^{-3}$ regime in terms of the GT results) are significantly deviated at all sites. In contrast our π SRGAN achieves a substantial improvement compared to the SRGAN, showing an accuracy comparable to that of the CDFDM. We remark on the discrepancies observed for tails in the large precipitation (small probability of $P^{\text{GT}}(p) < 10^{-5}$) regime even in the cases of the CDFDM and π SRGAN. These rare events corresponding to disaster-level torrential rains are very important from the perspective of disaster prevention but are beyond the limit of the current statistical DS methods, on which we provide an overview in the concluding remarks.

Next we further quantify the performance of each method using the Kullback–Leibler divergence D_{KL} :

$$D_{\text{KL}}(P^{\text{GT}} || P^{\text{DS}}) \equiv \int dp P^{\text{GT}}(p) \log \frac{P^{\text{GT}}(p)}{P^{\text{DS}}(p)}, \quad (1)$$

where $P^{\text{GT}}(p)$ is the PDF of the GT and $P^{\text{DS}}(p)$ is that calculated using the downscaling results ($DS \in \{\pi\text{SRGAN}, \text{SRGAN}, \text{CDFDM}\}$). Generally, the more different $P^{\text{GT}}(p)$ and $P^{\text{DS}}(p)$ are, the larger D_{KL} becomes; D_{KL} vanishes when the two PDFs are exactly the

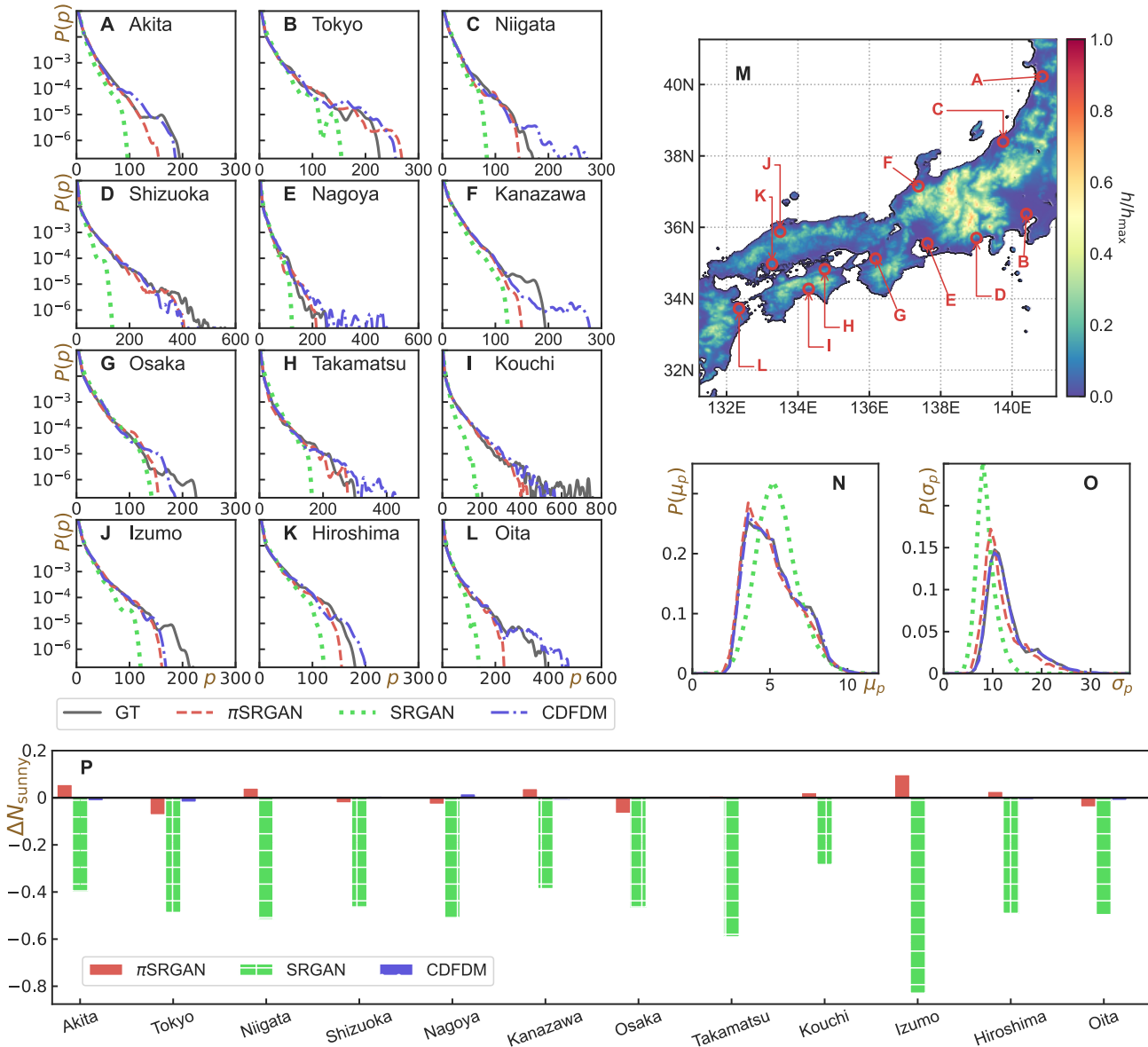


FIG. 3. Statistics of precipitation. (A-L) The probability distribution functions (PDFs) $P(p)$ as a function of the precipitation p at each site. 12 representative sites are chosen from all over Japan. The different ranges of the abscissa reflect the regional characteristics. See SI Appendix for the technical details in processing the PDFs. (M) The normalized topographic information and the locations of 12 sites of panels (A-L). (N,O) The PDFs of the mean μ_p and standard deviation σ_p of the precipitation over all the test data at each site; here the values of μ_p and σ_p at different sites serve as samples of the PDFs. (P) The relative error of the number of the sunny days.

same. Since the difference between two PDFs, $P^{\text{GT}}(p)$ and $P^{\text{DS}}(p)$, is weighted by the ground truth distribution, the KL divergence places more importance on the frequently occurring events than on rare events. Technical details such as the data preprocessing employed are provided in SI Appendix. The KL divergence between the GT and DS results using distinct methods are summarized in Table II D, where the values averaged over the 12 sites considered in Fig. 3 are presented. The values of D_{KL} for each single site are provided in Table S4. As

expected from the fact that the CDFDM concentrates on matching these statistics for the training data, it gives the best values for all cases. Remarkably, compared to the original SRGAN, the π SRGAN reduces D_{KL} down to the same order as that for the CDFDM, which is more than one order of magnitude smaller than that of SRGAN. These results are comparable to the CDFDM, allowing us to conclude that the π SRGAN achieves incredible accuracy.

TABLE II. Average KL divergence of PDFs

	π SRGAN	SRGAN	CDFDM
D_{KL}	3.28×10^{-3}	3.73×10^{-2}	1.31×10^{-3}

E. Statistics over all sites

We further measure the statistics over all sites: the PDFs of the mean μ_p and the standard deviation σ_p of the precipitation calculated over all test data on each pixel l :

$$\mu_p(l) \equiv \frac{1}{N_{\text{test}}} \sum_k^{N_{\text{test}}} p_k(l), \quad (2)$$

$$\sigma_p(l) \equiv \sqrt{\frac{1}{N_{\text{test}}} \sum_k^{N_{\text{test}}} (p_k(l) - \mu_p(l))^2}, \quad (3)$$

where $k \in \mathcal{D}_{\text{test}}$ is again the sample index, and N_{test} is the number of samples in $\mathcal{D}_{\text{test}}$. The probability distribution of μ_p and σ_p , denoted by $P(\mu_p)$ and $P(\sigma_p)$, are shown in Fig. 3(N,O). Note that here the values calculated on each pixel serve as samples for these PDFs.

High accuracy comparable to the CDFDM is obtained for $P(\mu_p)$ of π SRGAN. Here, we remark again that the almost identical results of the CDFDM to those of the GT are expected because the data are reconstructed such that the PDFs become totally consistent with those of the training data. The total shift to the left of the $P(\sigma_p)$ of the π SRGAN is a consequence of the underestimation of the high-precipitation events shown in Fig. 3(A-L); μ_p tends to be slightly smaller than the GT, and thus, σ_p becomes systematically smaller. Interestingly, while SRGAN underestimates the frequency of the high precipitation events much worse than π SRGAN, its $P(\mu_p)$ shifts toward the large p value side. This reflects the fact that in the results of SRGAN, the number of sunny days is very small and, instead, there are a great number of days with low precipitation. We clarify this in Fig. 3P, which presents the relative error of the number of sunny days $\Delta N_{\text{sunny}} = (N_{\text{sunny}}^{DS} - N_{\text{sunny}}^{\text{GT}})/N_{\text{sunny}}^{\text{GT}}$, where N_{sunny}^{DS} and $N_{\text{sunny}}^{\text{GT}}$ are the number of sunny days in each data set. Here, sunny is defined as precipitation less than 1 mm/day. The plot clearly shows that SRGAN tends to underestimate N_{sunny} largely, whereas we observe a clear improvement in terms of ΔN_{sunny} for π SRGAN.

F. Spatial correlation

Here, we examine in detail the spatial correlation of the downscaled results. The importance of the spatial correlation of the meteorological variables, i.e., the relation between two distant sites, has been realized very recently [13–17], e.g., in the context of impact assessment

of climate change. However, conventional DS methods such as CDFDM have proven to overestimate the correlation even though the statistical consistency with the GT is maintained [26–28]. Such a tendency is actually seen in the qualitative visualizations in Fig. 2, where the overly smoothed profiles are obtained. We thus systematically evaluate the accuracy in expressing the spatial correlation of the precipitation by measuring the Pearson’s correlation coefficients of the precipitation $C_M^R(l, l')$ between two sites, l and l' , which is defined as:

$$C_M(l, l') = \left\langle \frac{\frac{1}{N_M} \sum_k^{N_M} (\delta p_k(l) \delta p_k(l'))}{\sqrt{\frac{1}{N_M} \sum_k^{N_M} (\delta p_k(l))^2} \sqrt{\frac{1}{N_M} \sum_k^{N_M} (\delta p_k(l'))^2}} \right\rangle_M \quad (4)$$

where $\delta p_k^R(l) \equiv p_k^R(l) - \bar{p}_k^R(l)$ is the deviation of the k -th sample at site l from its reference average value $\bar{p}_k^R(l)$. The subscript M indicates that the average is taken over the data of month M and N_M represents the total number of test data samples belonging to month M . Since the distribution of the correlation coefficients is known to have features specific to each month, we measure the monthly values of the coefficients. Below, we focus on the results for $M = \text{January}$, for which a previous work has pointed out the existence of a distinguished spatial pattern of precipitation correlation [28].

Figures 4(A-C) show the spatial distribution of the correlation coefficients $C_{\text{Jan}}^R(l, l')$, with Nagoya, Niigata, and Hiroshima being the reference points l (the locations of the reference points are marked by the star symbols). The correlations measured for the CDFDM are too high compared to the GT at almost all sites, as shown in Fig. 4(A). This is because the 2500 grid points extracted from the corresponding single low-resolution pixel tend to have similar values. In contrast, the results of SRGAN and π SRGAN exhibit much sharper spatial contrast, e.g., the contrast between the north and south sides of the Chugoku area (around [36°N, 135°E]) is well captured. Comparing the results of SRGAN and π SRGAN, we further observe a clear distinction in the east-west contrast in the Tohoku area (around [38°N, 140°E]): the color varies as sharply as the GT in the case of π SRGAN and not in the SRGAN. In Fig. 4(B,C), we qualitatively observe the same difference in the accuracy among the methods. In particular, π SRGAN successfully reproduces even the nonmonotonic nature of the correlation as a function of the distance from the reference site: e.g., in the results of the GT and SRGAN-based methods in Fig. 4(B), along the north side coastline (see the arrow in the figure), the correlation decays quickly near the reference point and then grows again around the Noto peninsula (around [38°N, 137.5°E]). The CDFDM, on the other hand, merely exhibits the monotonic decay of the correlation along the same line.

To quantify the accuracy of $C_{\text{Jan}}^{SR}(l, l')$ for the different methods, we measure the mean square error (MSE) of the spatial distribution of the correlation coefficient defined

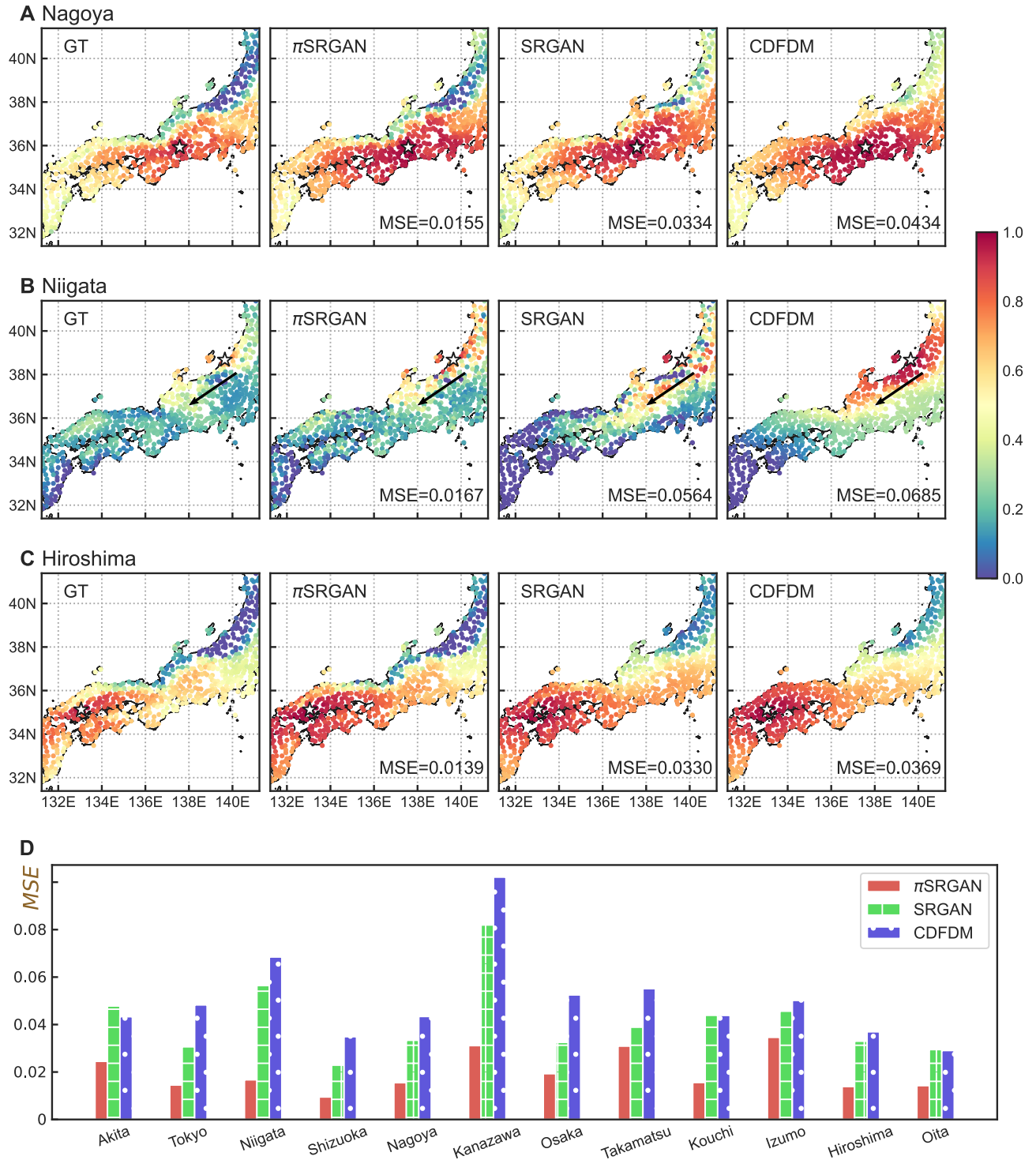


FIG. 4. Spatial distribution of the correlation coefficients for precipitation. The distributions of January obtained with the π SRGAN, SRGAN and CDFDM are compared against the ground truth (GT) in the case of the reference point of correlation at Nagoya [35.1667°N, 136.965°E] (A), Niigata [37.9133°N, 139.0483°E] (B), and Hiroshima [34.365°N, 132.4333°E] (C). The dot color indicates the values of $C_{\text{Jan}}^R(l, l')$ between the location of the dots and the reference site. The reference points are represented by star symbols. (D) The mean square error (MSE) of the correlation coefficients of the downscaled precipitations from those of the ground truth.

TABLE III. Average MSE of the correlation coefficients

	π SRGAN	SRGAN	CDFDM
MSE_{Jan}^{SR}	2.00×10^{-2}	4.14×10^{-2}	5.07×10^{-2}

as:

$$MSE_M^{SR}(l) = \frac{1}{N_{OS}} \sum_{l'}^{N_{OS}} (C_M^{SR}(l, l') - C_M^{GT}(l, l'))^2, \quad (5)$$

where l is the reference site and $N_{OS} \equiv 630$ is the number of observation stations (see SI Appendix). The values of MSE_{Jan}^{SR} measured based on each reference site are compared in Fig. 4(D), and the average values are listed in Table II F (the values for each site are shown in Table S4). The π SRGAN outperforms the SRGAN and the CDFDM for all sites considered here and achieves 2.5 times better accuracy than the CDFDM for the average value over 12 sites. This result of the GAN-based methods being advantageous in achieving the “naturalness” of the spatial pattern is consistent with the report in ref. [29]. Moreover, the difference in the results of π SRGAN and SRGAN solely derives from the introduction of the sea level pressure field (the SRGAN used in this work is aware of the topographic information: see Method section). This indicates that the pressure field effectively serves as the crucial information for the precipitation projection, such as the location of the frontogenesis. Together with the discussion in the previous subsections, this result enables us to conclude that the present π SRGAN has the ability to reproduce both the statistical properties and spatial correlation, which highlight the applicability to local-scale and interregional assessments of climate change.

III. DISCUSSION

We have developed a machine learning-based statistical downscaling (DS) method with a large scale-factor of fifty, while maintaining both the basic statistical properties and the spatial correlation. We employed a physics-informed type approach [31] on the basis of the SRGAN-based method, and specifically, we developed a framework to use the proper auxiliary physical information along with the low-resolution input to attain large improvements in the DS performance as summarized in Fig. 1 and Tables II D, II F. High accuracy comparable to the CDFDM, a conventional method in actual use, was demonstrated by directly comparing the climatological statistical properties with the real data. More importantly, our approach exhibited the highly accurate reconstruction given in Fig. 4 of the natural spatial distribution of the precipitation correlation coefficient, which was a serious issue for the conventional statistical DS methods, including CDFDM [26–28]. Since the importance of the multiregional spatial correlation has recently been

recognized [13–17], the present method is a promising new-generation alternative to conventional statistical DS methods, particularly in situations where the integration of the multiregional information is necessary.

The detection and prediction of rare events are vital issues *inter alia* in the context of climate change assessments. The methods including the present π SRGAN indeed have yet to accurately capture the low probability but significant rainfalls, as shown in Fig. 3. Here, we discuss possible directions to ameliorate the problem. First, we could raise the level of physics-informed machine learning in terms of the classification proposed in ref. [31]. If we succeeded in directly incorporating directly some part of the governing equations into the learning process while maintaining the computational efficiency, local phenomena such as heavy rains would be predicted with high reliability. Another direction is to take measures to reform the basic machine learning architecture itself. Following the GAN-based approach, flow-based and diffusion model-based methods have attracted public attentions as powerful next-generation tools for general super-resolution tasks [43, 44]. The main feature of these approaches is to generate multiple image candidates from a single input. Therefore, probabilistic information is expected to be drawn from the multiple super-resolved images, which would enable us to tackle the rare event predictions.

Another perspective concerns the use of machine learning techniques to improve the efficiency of dynamical downscaling, i.e., developing a high-speed machine-learning-based solver for the governing equations of climate models. Here we refer to an example of a speed up of multiscale simulations; in ref. [45] the Gaussian process is used to reduce the computational burden of multiscale simulation for polymeric liquid to achieve a reduction by a factor of 30-100 without loss of accuracy. Breakthroughs driven by similar approaches are expected once the complexity of the governing equations for the climate models is overcome.

IV. METHODS

A. CDFDM

Among a variety of statistical methods, we use, as a reference, the cumulative distribution function-based downscaling method (CDFDM) with quantile mapping that is in actual use.

If we simply map the low-resolution GCM simulation results onto the point at which the observations are available, we generally see a systematic difference, defined as bias, which comes from the systematic error of the model prediction and/or from the interpolation error. Removing this inherent bias is especially important in applying the downscaling results to the impact assessments. In the CDFDM, bias is corrected via an empirical transfer function constructed in advance using measured data

of distributional variables and the corresponding simulation results. The detailed procedure of constructing the transfer function is described as follows [34].

The crude low-resolution data obtained from the GCM are first mapped onto a 2 km mesh using simple bilinear interpolation. At each mesh point, an empirical cumulative distribution function (CDF) is then constructed using the interpolated data of the variable of interest over a specified time window. The transfer function is defined as a map of a variable onto the one at which the corresponding CDF of the observation falls within the same quantile level. This preconstructed transfer function is applied under the assumption that the error-percentile relation is conserved over time. In the present study, the time window of a month is employed, while the original time window is over a half-year [34], to more sensitively capture the seasonal trend [46, 47].

Note that while this CDFDM is a nonparametric method, the corrected CDF perfectly matches the corresponding CDF of the observation (for the training data); the statistical properties of the downscaling results are expected to reproduce the observation well. The bias-corrected climate scenario obtained with this method has been widely used in climate change impact studies [46, 48, 49].

B. SRGAN

We employ a generative adversarial networks-based (GAN-based) method as the basic machine learning architecture, which is called Super-Resolution Generative Adversarial networks (SRGAN) [50]. The terminology super-resolution (SR; or, in particular, single-image super-resolution) refers to a method of restoring a high-resolution image from the corresponding low-resolution data and is the counterpart of the downscaling in the

realm of the general image processing. The GAN-based methods are capable of generating realistic images by pitting a discriminator network against a generator network that generates samples (see Fig. 1A). The discriminator network takes the real data (ground truths) and the fake data (output of the generator network) as inputs and identifies the authenticity of the input samples. The generator network tries to deceive the discriminator while the discriminator tries to judge with high accuracy. As a result, both networks spontaneously learn the “realistic” information. The SRGAN can reproduce fine textures that cannot be achieved by normal convolutional neural network-based variants and offers substantially improved realistic super-resolution images.

Such network-based super-resolution techniques have recently been used for the DS tasks of climatological data. In a representative report by Stengel and coworkers, ref. [29], the authors compared the performances of SRGAN-based downscaling methods with previous methods (SRCNN: Super-Resolution Convolutional Neural Networks). Although the SRCNN-based method appeared to be superior in evaluating the performance in terms of the simple pixelwise MSE, the SRGAN-based method provided *realistic* results satisfying the important physical requirements, e.g., the energy spectrum of the wind velocity field satisfied the Kolmogorov 5/3 scaling law [35] with remarkable accuracy. The network architecture in our π SRGAN is mostly the same as the original SRGAN introduced in ref. [50], although the batch normalization layers are removed obeying ref. [29]: the precise architecture is presented in Fig. S1. We also summarize other technical details, such as the precise learning protocol or the normalization of the data, in SI Appendix. We note that the representative method compared to the π SRGAN referred to as “SRGAN” in our implementation is a slightly upgraded version including the high-resolution topography, which makes possible the decomposition of elements producing the improvement.

-
- [1] S.-K. Min, X. Zhang, F. W. Zwiers, G. C. Hegerl, Human contribution to more-intense precipitation extremes. *Nature* **470**, 378–381 (2011).
 - [2] P. Pall, T. Aina, D. A. Stone, P. A. Stott, T. Nozawa, A. G. J. Hilberts, D. Lohmann, M. R. Allen, Anthropogenic greenhouse gas contribution to flood risk in England and Wales in autumn 2000. *Nature* **470**, 382–385 (2011).
 - [3] H. Kawase, Y. Imada, H. Sasaki, T. Nakaegawa, A. Murata, M. Nosaka, I. Takayabu, Contribution of Historical Global Warming to Local-Scale Heavy Precipitation in Western Japan Estimated by Large Ensemble High-Resolution Simulations. *Journal of Geophysical Research: Atmospheres* **124**, 6093–6103 (2019).
 - [4] Y. Imada, H. Kawase, M. Watanabe, M. Arai, H. Shioyama, I. Takayabu, Advanced risk-based event attribution for heavy regional rainfall events. *npj Climate and Atmospheric Science* **3**, 37 (2020).
 - [5] V. Masson-Delmotte, P. Zhai, A. Pirani, S. L. Connors, C. Péan, S. Berger, N. Caud, Y. Chen, L. Goldfarb, M. Gomis, *et al.*, Climate change 2021: the physical science basis. *Contribution of working group I to the sixth assessment report of the intergovernmental panel on climate change* p. 2 (2021).
 - [6] K. Sudo, M. Takahashi, J.-i. Kurokawa, H. Akimoto, CHASER: A global chemical model of the troposphere 1. Model description. *Journal of Geophysical Research: Atmospheres* **107**, ACH 7–1–ACH 7–20 (2002).
 - [7] H. Sato, A. Itoh, T. Kohyama, SEIB-DGVM: A new Dynamic Global Vegetation Model using a spatially explicit individual-based approach. *Ecological Modelling* **200**, 279–307 (2007).
 - [8] M. Watanabe, T. Suzuki, R. O’ishi, Y. Komuro, S. Watanabe, S. Emori, T. Takemura, M. Chikira, T. Ogura, M. Sekiguchi, K. Takata, D. Yamazaki, T. Yokohata, T. Nozawa, H. Hasumi, H. Tatebe, M. Ki-

- moto, Improved Climate Simulation by MIROC5: Mean States, Variability, and Climate Sensitivity. *Journal of Climate* **23**, 6312–6335 (2010).
- [9] S. YUKIMOTO, Y. ADACHI, M. HOSAKA, T. SAKAMI, H. YOSHIMURA, M. HIRABARA, T. Y. TANAKA, E. SHINDO, H. TSUJINO, M. DEUSHI, R. MIZUTA, S. YABU, A. OBATA, H. NAKANO, T. KOSHIRO, T. OSE, A. KITO, A New Global Climate Model of the Meteorological Research Institute: MRI-CGCM3 —Model Description and Basic Performance—. *Journal of the Meteorological Society of Japan. Ser. II* **90A**, 23–64 (2012).
- [10] G. A. Schmidt, M. Kelley, L. Nazarenko, R. Ruedy, G. L. Russell, I. Aleinov, M. Bauer, S. E. Bauer, M. K. Bhat, R. Bleck, V. Canuto, Y.-H. Chen, Y. Cheng, T. L. Clune, A. Del Genio, R. de Fainchtein, G. Faluvegi, J. E. Hansen, R. J. Healy, N. Y. Kiang, D. Koch, A. A. Lacis, A. N. LeGrande, J. Lerner, K. K. Lo, E. E. Matthews, S. Menon, R. L. Miller, V. Oinas, A. O. Oloso, J. P. Perlwitz, M. J. Puma, W. M. Putman, D. Rind, A. Romanou, M. Sato, D. T. Shindell, S. Sun, R. A. Syed, N. Tausnev, K. Tsigaridis, N. Unger, A. Voulgarakis, M.-S. Yao, J. Zhang, Configuration and assessment of the GISS ModelE2 contributions to the CMIP5 archive. *Journal of Advances in Modeling Earth Systems* **6**, 141–184 (2014).
- [11] P. A. Stott, S. F. B. Tett, G. S. Jones, M. R. Allen, J. F. B. Mitchell, G. J. Jenkins, External Control of 20th Century Temperature by Natural and Anthropogenic Forcings. *Science* **290**, 2133–2137 (2000).
- [12] E. Scoccimarro, S. Gualdi, A. Bellucci, A. Sanna, P. Giuseppe Fogli, E. Manzini, M. Vichi, P. Oddo, A. Navarra, Effects of Tropical Cyclones on Ocean Heat Transport in a High-Resolution Coupled General Circulation Model. *Journal of Climate* **24**, 4368–4384 (2011).
- [13] N. C. Onat, M. Kucukvar, Carbon footprint of construction industry: A global review and supply chain analysis. *Renewable and Sustainable Energy Reviews* **124**, 109783 (2020).
- [14] D. Ivanova, J. Barrett, D. Wiedenhofer, B. Macura, M. Callaghan, F. Creutzig, Quantifying the potential for climate change mitigation of consumption options. *Environmental Research Letters* **15**, 093001 (2020).
- [15] X. Fu, M. Lahr, Z. Yaxiong, B. Meng, Actions on climate change, reducing carbon emissions in china via optimal interregional industry shifts. *ENERGY POLICY* **102**, 616–638 (2017).
- [16] X. Zhao, X. Wu, C. Guan, R. Ma, C. P. Nielsen, B. Zhang, Linking Agricultural GHG Emissions to Global Trade Network. *Earth's Future* **8** (2020).
- [17] E. E. Koks, M. Thissen, A Multiregional Impact Assessment Model for disaster analysis. *Economic Systems Research* **28**, 429–449 (2016).
- [18] F. Giorgi, G. T. Bates, The Climatological Skill of a Regional Model over Complex Terrain. *Monthly Weather Review* **117**, 2325–2347 (1989).
- [19] Y. WANG, L. R. LEUNG, J. L. MCGREGOR, D.-K. LEE, W.-C. WANG, Y. DING, F. KIMURA, Regional Climate Modeling: Progress, Challenges, and Prospects. *Journal of the Meteorological Society of Japan. Ser. II* **82**, 1599–1628 (2004).
- [20] M. Déqué, R. G. Jones, M. Wild, F. Giorgi, J. H. Christensen, D. C. Hassell, P. L. Vidale, B. Rockel, D. Jacob, E. Kjellström, M. de Castro, F. Kucharski, B. van den Hurk, Global high resolution versus Limited Area Model climate change projections over Europe: quantifying confidence level from PRUDENCE results. *Climate Dynamics* **25**, 653–670 (2005).
- [21] H. Kawase, T. Yoshikane, M. Hara, B. Ailikun, F. Kimura, T. Yasunari, Downscaling of the Climatic Change in the Mei-yu Rainband in East Asia by a Pseudo Climate Simulation Method. *SOLA* **4**, 73–76 (2008).
- [22] H. von Storch, E. Zorita, U. Cubasch, Downscaling of Global Climate Change Estimates to Regional Scales: An Application to Iberian Rainfall in Wintertime. *Journal of Climate* **6**, 1161–1171 (1993).
- [23] R. L. Wilby, S. P. Charles, E. Zorita, B. Timbal, P. Whetton, L. O. Mearns, Guidelines for use of climate scenarios developed from statistical downscaling methods. *Supporting material of the Intergovernmental Panel on Climate Change, available from the DDC of IPCC TGCIA* **27** (2004).
- [24] C. Piani, J. O. Haerter, E. Coppola, Statistical bias correction for daily precipitation in regional climate models over Europe. *Theoretical and Applied Climatology* **99**, 187–192 (2010).
- [25] T. Iizumi, M. Nishimori, K. Dairaku, S. A. Adachi, M. Yokozawa, Evaluation and intercomparison of down-scaled daily precipitation indices over Japan in present-day climate: Strengths and weaknesses of dynamical and bias correction-type statistical downscaling methods. *Journal of Geophysical Research* **116**, D01111 (2011).
- [26] D. Maraun, T. G. Shepherd, M. Widmann, G. Zappa, D. Walton, J. M. Gutiérrez, S. Hagemann, I. Richter, P. M. M. Soares, A. Hall, L. O. Mearns, Towards process-informed bias correction of climate change simulations. *Nature Climate Change* **7**, 764–773 (2017).
- [27] M. Widmann, J. Bedia, J. M. Gutiérrez, T. Bosshard, E. Hertig, D. Maraun, M. J. Casado, P. Ramos, R. M. Cardoso, P. M. M. Soares, J. Ribalaygua, C. Pagé, A. M. Fischer, S. Herrera, R. Huth, Validation of spatial variability in downscaling results from the VALUE perfect predictor experiment. *International Journal of Climatology* p. joc.6024 (2019).
- [28] N. Ishizaki, To be published .
- [29] K. Stengel, A. Glaws, D. Hettlinger, R. N. King, Adversarial super-resolution of climatological wind and solar data. *Proceedings of the National Academy of Sciences* **117**, 16805–16815 (2020).
- [30] J. Cheng, J. Liu, Q. Kuang, Z. Xu, C. Shen, W. Liu, K. Zhou, Deepdt: Generative adversarial network for high-resolution climate prediction. *IEEE Geoscience and Remote Sensing Letters* **19**, 1–5 (2022).
- [31] R. Onishi, D. Sugiyama, K. Matsuda, Super-Resolution Simulation for Real-Time Prediction of Urban Micrometeorology. *SOLA* **15**, 178–182 (2019).
- [32] H. OHNO, K. SASAKI, G. OHARA, K. NAKAZONO, Development of grid square air temperature and precipitation data compiled from observed, forecasted, and climatic normal data. *Climate in Biosphere* **16**, 71–79 (2016).
- [33] Y. HARADA, H. KAMAHORI, C. KOBAYASHI, H. ENDO, S. KOBAYASHI, Y. OTA, H. ONODA, K. ONOGI, K. MIYAOKA, K. TAKAHASHI, The JRA-55 Reanalysis: Representation of Atmospheric Circulation and Climate Variability. *Journal of the Meteorological Society of Japan. Ser. II* **94**, 269–302 (2016).
- [34] T. IIZUMI, M. NISHIMORI, Y. ISHIGOOKA,

- M. YOKOZAWA, Introduction to climate change scenario derived by statistical downscaling. *Journal of Agricultural Meteorology* **66**, 131–143 (2010).
- [35] U. Frisch, *Turbulence* (Cambridge University Press, 1995).
- [36] T. Vandal, E. Kodra, S. Ganguly, A. Michaelis, R. Nemani, A. R. Ganguly, *Proceedings of the 23rd ACM SIGKDD International Conference on Knowledge Discovery and Data Mining*, KDD '17 (Association for Computing Machinery, New York, NY, USA, 2017), p. 1663–1672.
- [37] T. Vandal, E. Kodra, S. Ganguly, A. Michaelis, R. Nemani, A. R. Ganguly, *Proceedings of the Twenty-Seventh International Joint Conference on Artificial Intelligence, IJCAI-18* (International Joint Conferences on Artificial Intelligence Organization, 2018), pp. 5389–5393.
- [38] Y. Yasuda, R. Onishi, Y. Hirokawa, D. Kolomenskiy, D. Sugiyama, Super-resolution of near-surface temperature utilizing physical quantities for real-time prediction of urban micrometeorology (2021).
- [39] D. Maraun, M. Widmann, *Statistical Downscaling and Bias Correction for Climate Research* (Cambridge University Press, 2018).
- [40] H. von Storch, E. Zorita, U. Cubasch, Downscaling of Global Climate Change Estimates to Regional Scales: An Application to Iberian Rainfall in Wintertime. *Journal of Climate* **6**, 1161–1171 (1993).
- [41] R. Huth, Statistical downscaling in central Europe: evaluation of methods and potential predictors. *Climate Research* **13**, 91–101 (1999).
- [42] G. Dayon, J. Boé, E. Martin, Transferability in the future climate of a statistical downscaling method for precipitation in France. *Journal of Geophysical Research: Atmospheres* **120**, 1023–1043 (2015).
- [43] A. Lugmayr, M. Danelljan, L. Van Gool, R. Timofte, SRFlow: Learning the Super-Resolution Space with Normalizing Flow (SRFlow, 2020), pp. 715–732.
- [44] H. Li, Y. Yang, M. Chang, S. Chen, H. Feng, Z. Xu, Q. Li, Y. Chen, SRDiff: Single image super-resolution with diffusion probabilistic models. *Neurocomputing* **479**, 47–59 (2022).
- [45] N. Seryo, T. Sato, J. J. Molina, T. Taniguchi, Learning the constitutive relation of polymeric flows with memory. *Physical Review Research* **2**, 33107 (2020).
- [46] T. Yokohata, G. Iwahana, T. Sone, K. Saito, N. N. Ishizaki, T. Kubo, H. Oguma, M. Uchida, Projections of surface air temperature required to sustain permafrost and importance of adaptation to climate change in the Daisetsu Mountains, Japan. *Scientific Reports* **11**, 15518 (2021).
- [47] N. N. Ishizaki, H. SHIOGAMA, N. Hanasaki, K. Takahashi, Development of cmip6-based climate scenarios for japan using statistical method and their applicability to impact studies. *Earth and Space Science Open Archive* p. 16 (2022).
- [48] Y. Hiruta, N. N. Ishizaki, S. Ashina, K. Takahashi, Regional and temporal variations in the impacts of future climate change on Japanese electricity demand: Simultaneous interactions among multiple factors considered. *Energy Conversion and Management: X* **14**, 100172 (2022).
- [49] Y. Hiruta, N. N. Ishizaki, S. Ashina, K. Takahashi, Hourly future climate scenario datasets for impact assessment of climate change considering simultaneous interactions among multiple meteorological factors. *Data in Brief* **42**, 108047 (2022).
- [50] C. Ledig, L. Theis, F. Huszár, J. Caballero, A. Cunningham, A. Acosta, A. Aitken, A. Tejani, J. Totz, Z. Wang, W. Shi, Photo-realistic single image super-resolution using a generative adversarial network. *Proceedings - 30th IEEE Conference on Computer Vision and Pattern Recognition, CVPR 2017* **2017-Janua**, 105–114 (2017).

V. ACKNOWLEDGMENTS

The authors thank N. Hanasaki and S. Koyama for fruitful discussions. This research was partially supported by JST Grant Number JPMJPF2013.

Deep generative model super-resolves spatially correlated multiregional climate data— supplemental material

Norihiro Oyama,^{1,*} Noriko N. Ishizaki,² Satoshi Koide,¹ and Hiroaki Yoshida¹

¹Toyota Central R&D Labs, Inc., Bunkyo-ku, Tokyo 112-0004, Japan

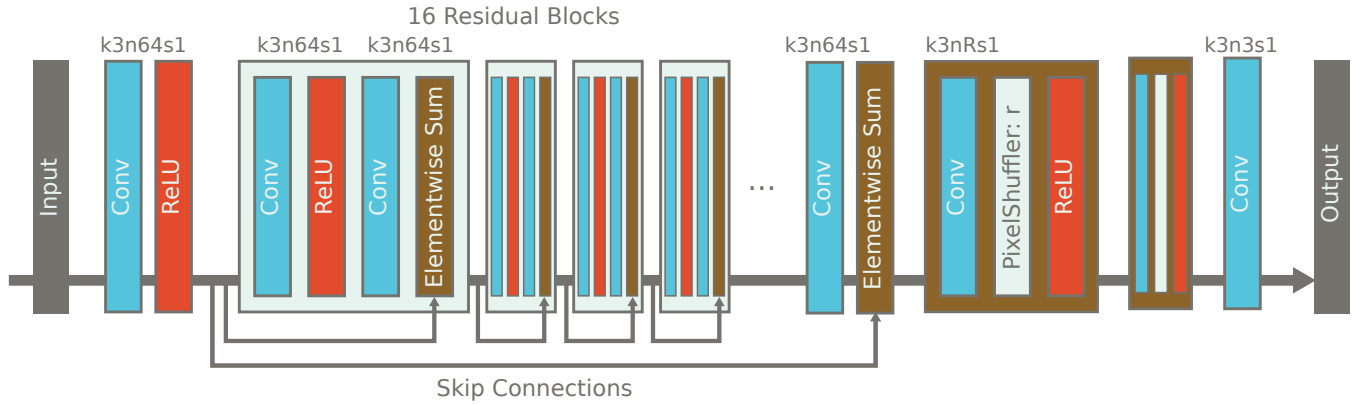
²Center for Climate Change Adaptation, National Institute for Environmental Studies, Tsukuba 305-8506, Japan.

I. TECHNICAL DETAILS

A. Architectures of networks

The network architecture is depicted in Fig. S1. In this figure, *Conv* stands for the convolution layer and *Dense* represents the fully connected layer. The numbers and alphabets above the Convs represent the hyperparameters: the numbers after k, n, and s are the kernel size, the number of kernels, and the stride, respectively. The number of kernels in the pixel shuffle layers R is determined by the scale factor r as $R = 64 \times r^2$. There can be multiple pixel shuffle layers if the scale factor can be factorizable (in that case, each pixel shuffle layer has a factorized prime number value as the scale factor, e.g., 2 and 5 if the scale factor is 10). All Leaky ReLU layers in the discriminator network employ the slope of 0.2 for negative inputs. We introduced special processing in the input layer of the generator network to concatenate the high-resolution topographic information with other low-resolution information. This special treatment will be explained in Sec. ID later.

Generator Network



Discriminator Network

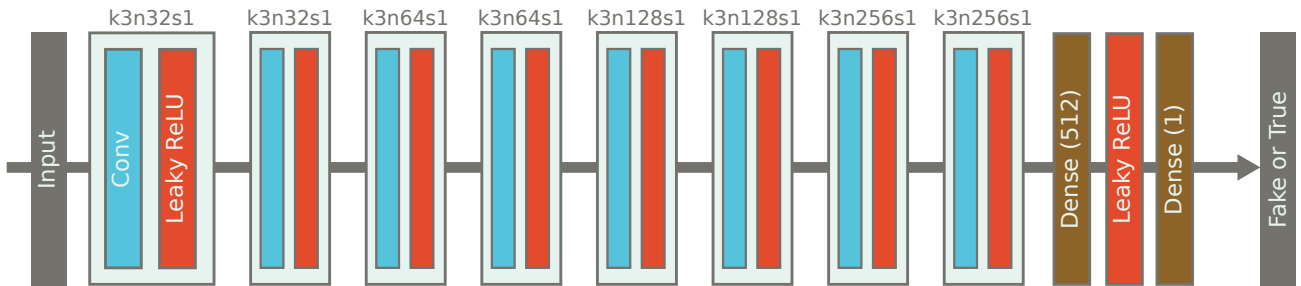


FIG. S1. Schematic pictures of the architectures of the generator and discriminator networks.

* Norihiro.Oyama.vb@mosk.tytlabs.co.jp

B. Learning protocol

In this section, we explain the details of the learning protocol. The protocol basically obeys ref. [1]. The fifty-fold downscaling is composed of two stages: the low-resolution to medium-resolution (LR-to-MR) and the medium-resolution to high-resolution (MR-to-HR) downscaling stages. The scale factors for these two stages are ten- and fivefold, respectively, and a fifty-fold scaling factor is achieved overall. The MR ground truths for the learning are generated by coarse-graining the HR image (average pooling with the kernel of size 5 and the stride is set to 5). We also introduced pretraining for the Generator network as usual. In total, there are four stages of learning: pretraining and GAN training for both LR-to-MR and MR-to-HR downscaling. We summarize the number of epochs and the batch size for each training stage in Table S1. The same value of the initial learning rate, $r_l = 10^{-4}$, is employed for all learning stages, and the learning rate is multiplied by 0.99 every epoch. Under this exponentially decreasing-learning-rate protocol, the learning rate becomes approximately one tenth every 230 steps. We confirmed that these setups prevent the system from overtraining with the epoch numbers we employed.

TABLE S1. Epoch number and batch size for each training state

	LR to MR		MR to HR	
	pre-training	GAN	pre-training	GAN
Epoch number	2000	500	500	100
Batch size	100	100	50	5

Regarding the loss function, again, we obeyed ref. [1]. We employed the simple MSE loss \mathcal{L}_{MSE} for the pretraining regardless of the resolution stages. For the loss of the Generator network in the GAN part \mathcal{L}_{G} , we use the linear combination of \mathcal{L}_{MSE} and the adversarial loss \mathcal{L}_{Adv} :

$$\mathcal{L}_{\text{G}} = \mathcal{L}_{\text{MSE}} + \alpha \mathcal{L}_{\text{Adv}}, \quad (\text{S1})$$

where α is the weight of the adversarial contribution and we set it as $\alpha = 0.001$ in this work. The adversarial loss represents the (in)accuracy of the discriminator classification of the outputs of the Generator (into fake and true). For \mathcal{L}_{Adv} , ref. [1] provides the detailed definition. It is considered that the information can be extracted most efficiently from the Discriminator when the discriminator loss \mathcal{L}_{D} is around 0.5. In this work, to maintain the value of \mathcal{L}_{D} in the vicinity of 0.5, adaptive training is carried out. In this special training protocol, the training for the discriminator is repeated if \mathcal{L}_{D} is larger than 0.6 and that for the generator recurs if \mathcal{L}_{D} is less than 0.45. Although in many cases such adaptive loops are performed for each minibatch, in this work, the adaptive loops are over the whole dataset. We have employed these precise protocols because we found them to be better than other options, after trials and errors.

C. Normalization of the data

All the data used for the training are normalized so that most (not all: see below) resulting pixels are in the interval $[0, 1]$. This is simply done by applying the following formula:

$$\tilde{x} = (x - x_{\text{lb}}) / x_{\text{scale}}, \quad (\text{S2})$$

where x denotes the variable of interest (one of the temperature, precipitation, sea-level pressure, or topography), \tilde{x} is the normalized value, and x_{lb} and x_{scale} are the lower bound and the scale of the variable x , respectively. The precise values of x_{lb} and x_{scale} for each variable are summarized in Table S2. Such normalization is known to enhance the training efficiency. We stress that for precipitation, this normalization does not guarantee that all the resulting values are less than unity since rare events exceed the threshold value of 100mm/day .

D. Input information processing

In our method, we concatenate the high-resolution topographic information with other low-resolution data, i.e., temperature, precipitation, and sea-level pressure. To combine such information with different resolutions in a consistent manner, we introduced special processing in the input layer of the generator, as mentioned in Sec. IA.

TABLE S2. The parameters used for the data normalization

	x_{lb}	x_{scale}
Temperature	-50K	100K
Precipitation	0 mm/day	100 mm/day
Sea level pressure	950 hPa	1050 hPa
Topography	0 m	4000 m

First, all low-resolution data are upsampled by simple bicubic interpolation. Then, we concatenate the resulting high-resolution data with the topographic information into an I -channeled two-dimensional image and downsample it by a convolution operation, where I is the number of input variables (temperature, precipitation, topography, and sea-level pressure for the LR-to-MR stage and only temperature, precipitation, and topography for the MR-to-HR stage). For this downsampling process, we used a kernel with a fixed size of 3 and set the stride to be the same value as the scale factor. Because, in our calculations, the scale factor of ten (for the LR-to-MR stage) is achieved by the succession of the twofold and fivefold processes, this special processing in the input layer of the LR-to-MR stage is composed of two convolution layers with parameters of k3nIs2 and k3nIs5. The resulting I channeled information is fed to the Generator network. Of course, the convolution kernels in this input layer are also trained during the learning process.

It is also important to mention that the accuracy is improved if the topography is simultaneously “downscaled”. (we omit the topography from the output in the schematic picture in Fig. 1 in the main text just because it is merely a guide, and not the downscaling target). We also note that the topography is introduced to the SRGAN as well. In this sense, what we call SRGAN in our case studies is not totally the same as the one introduced in ref. [1]. We introduced the topography in order to identify which of the topography and the sea level pressure is crucial information to improve the performance of SRGAN. Our results indicate that it is the sea level pressure field that changes the accuracy of the SRGAN significantly.

E. Precise measurement protocol of KL divergence

Technically, D_{KL} tends to infinity when $P^{GT}(x) \neq 0$ and $P^{SR}(x) = 0$ holds for a value x (or more technically speaking, for a bin including x), and vice versa. Problematically, this usually happens in real situations because of the limited number of samples: the probabilities of finding rare events are regarded as zero when the number of samples is finite even though they should be small but nonzero in the “true” distribution that is expected to be obtained when the sample number becomes infinite. This results in an undesired infinite value of D_{KL} . To avoid such a trivial artifact, we applied the Gaussian smoothing function $f(x) = \frac{1}{\sqrt{2\pi}w} \exp\left\{-\frac{(x)^2}{2w^2}\right\}$ as:

$$P(x) = \frac{1}{Z\Delta} \sum_i^N f(x - x_i), \quad (S3)$$

where w^2 is the variance of the Gaussian and determines the smoothing width, Z is the normalizing factor, Δ is the bin width, and N is the number of data. $P(x)$ gives the probability of finding a sample in the interval $[x - \frac{\Delta}{2}, x + \frac{\Delta}{2}]$ and x_i is the value of the sample i . We fixed this hyperparameter w^2 and Δ to be $w^2 = 16$ and $\Delta = 2$ to obtain the results presented in Fig. 3 and Table 2 in the main text and Table S4. We confirmed that a change in the value of w by a factor of 4 does not change the qualitative results.

F. Locations where the correlation coefficients are evaluated

If we calculate the correlations between all the 400×400 grid points, the calculation cost becomes very expensive. Therefore, we extracted only the grid points where the observation stations of the Automated Meteorological Data Acquisition System reside. There are $N_{OS} = 630$ stations within the system boundary of our study.

G. Topographic information

The precise topographic information about the locations considered in Fig. 3 is summarized in Table S3. The pixels within the region specified by the min/max of the latitude/longitude compose each site. Since, in our case studies, a single pixel in the high-resolution data has a linear dimension of 0.025 degrees in terms of both latitude and longitude, the regions of sites in Table S3 are all composed of 100 pixels.

TABLE S3. Precise information of the location of each site

	Latitude		Longitude	
	min	max	min	max
(A) Akita	39.475°N	39.725°N	140.1°E	140.35°E
(B) Tokyo	35.625°N	35.875°N	139.65°E	139.9°E
(C) Niigata	37.65°N	37.9°N	139.0°E	139.25°E
(D) Shizuoka	34.95°N	35.2°N	138.25°E	138.5°E
(E) Nagoya	34.8°N	35.05°N	136.875°E	137.125°E
(F) Kanazawa	36.4°N	36.65°N	136.625°E	136.875°E
(G) Osaka	34.375°N	34.625°N	135.425°E	135.675°E
(H) Takamatsu	34.075°N	34.325°N	134.0°E	134.25°E
(I) Kouchi	33.525°N	33.775°N	133.55°E	133.8°E
(J) Izumo	35.125°N	35.375°N	132.75°E	133.0°E
(K) Hiroshima	34.225°N	34.475°N	132.525°E	132.775°E
(L) Oita	32.975°N	33.225°N	131.6°E	131.85°E

II. PRECISE VALUES OF STATISTICAL INDICATORS

We summarize the precise values of D_{KL} and MSE_{Jan} for each site in Table S4

-
- [1] K. Stengel, A. Glaws, D. Hettinger, and R. N. King, Adversarial super-resolution of climatological wind and solar data, *Proceedings of the National Academy of Sciences* **117**, 16805 (2020).

TABLE S4. Values of KL divergence of PDFs and MSE of correlation coefficients

	D_{KL}			MSE_{Jan}		
	SRGAN	OURS	CDFDM	SRGAN	OURS	CDFDM
Akita	2.91×10^{-2}	3.23×10^{-3}	8.08×10^{-4}	4.78×10^{-2}	2.45×10^{-2}	4.33×10^{-2}
Tokyo	2.59×10^{-2}	2.71×10^{-3}	1.91×10^{-3}	3.06×10^{-2}	1.45×10^{-2}	4.83×10^{-2}
Niigata	3.09×10^{-2}	2.37×10^{-3}	1.12×10^{-3}	5.64×10^{-2}	1.67×10^{-2}	6.85×10^{-2}
Shizuoka	1.02×10^{-1}	2.07×10^{-3}	8.07×10^{-4}	2.29×10^{-2}	9.48×10^{-3}	3.49×10^{-2}
Nagoya	1.03×10^{-2}	2.80×10^{-3}	1.92×10^{-3}	3.34×10^{-2}	1.55×10^{-2}	4.34×10^{-2}
Kanazawa	2.50×10^{-2}	3.98×10^{-3}	8.87×10^{-4}	8.19×10^{-2}	3.11×10^{-2}	1.02×10^{-1}
Osaka	2.35×10^{-2}	2.66×10^{-3}	2.32×10^{-3}	3.25×10^{-2}	1.93×10^{-2}	5.25×10^{-2}
Takamatsu	4.44×10^{-2}	7.21×10^{-3}	9.97×10^{-4}	3.91×10^{-2}	3.09×10^{-2}	5.51×10^{-2}
Kouchi	8.19×10^{-2}	1.88×10^{-3}	1.10×10^{-3}	4.39×10^{-2}	1.56×10^{-2}	4.38×10^{-2}
Izumo	1.29×10^{-2}	1.92×10^{-3}	1.59×10^{-3}	4.56×10^{-2}	3.46×10^{-2}	5.02×10^{-2}
Hiroshima	1.79×10^{-2}	2.70×10^{-3}	1.17×10^{-3}	3.23×10^{-2}	1.39×10^{-2}	3.69×10^{-2}
Oita	4.32×10^{-2}	5.82×10^{-3}	1.07×10^{-3}	2.94×10^{-2}	1.43×10^{-2}	2.90×10^{-2}
Average	3.73×10^{-2}	3.28×10^{-3}	1.31×10^{-3}	4.14×10^{-2}	2.00×10^{-2}	5.07×10^{-2}

(the best values are shown in bold letters for each row, each indicator)